



Cite this: *New J. Chem.*, 2018, 42, 18381

Received 2nd September 2018,
Accepted 5th October 2018

DOI: 10.1039/c8nj04472d

rsc.li/njc

Enhancing formaldehyde oxidation on iridium catalysts using hydrogenated TiO₂ supports†

Hang Cheong Chan, Ting Chen, Lifang Xie, Yijin Shu and Qingsheng Gao *

As promising catalyst supports, hydrogenated metal-oxides can afford engineered surface architectures and electronic configurations to promote catalytic turnover on loading metals. Herein, hydrogenated TiO₂ (H-TiO₂) fabricated *via* NaBH₄ reduction is successfully introduced to boost the catalytic oxidation of formaldehyde (HCHO), which is one of the most common and harmful indoor volatile organic compounds. Distinct from the parent TiO₂, H-TiO₂ features enriched surface hydroxyls and enhanced metal-support interactions upon loading Ir, which are responsible for remarkable promotion in HCHO oxidation. In particular, the abundant hydroxyls on H-TiO₂ promote the generation of HCOO⁻, which is believed to be the rate-determining step in HCHO oxidation. This discovery is anticipated to pave the way for exploring high-performance metal catalysts on oxide supports *via* surface and interfacial engineering.

Introduction

As one of the most common and harmful indoor volatile organic compounds (VOCs), formaldehyde (HCHO) can cause health problems such as headaches, skin/eye irritation, chest pain, nasal tumors, *etc.*^{1,2} To satisfy stringent environmental regulations, great efforts have been made to remove HCHO.^{3–6} Catalytic oxidation to harmless H₂O and CO₂ is an effective method, in which the key is the choice of catalytic materials.⁶ Catalysts used in HCHO oxidation are mainly noble metals supported by oxides.⁷ On one hand, Pt has been extensively investigated and demonstrated owing to its high performance related to the valence states.^{8–13} As another important element in the Pt-group, Ir is also active in oxidation reactions owing to its largely-expanded d-bands with rich vacancies.^{14–17} However, extensive efforts are still desired to uncover its catalytic application and mechanism in formaldehyde oxidation. On the other hand, metal-oxide (*e.g.*, TiO₂, Fe₂O₃, ZrO₂, MnO_x-CeO₂, SnO₂, *etc.*) supports can promote the catalytic activity of loaded noble-metals.^{18–24} Besides their large surface that affords highly dispersed noble-metal centers, metal oxides more importantly provide available surface/interfacial interactions to enhance HCHO chemisorption and consequently the turnover.^{12,21,23,25} For example, Huang *et al.* reported on an efficient oxidation of HCHO on Pt/TiO₂ catalysts,²⁶ and the activity at room temperature was further improved after NaOH modification,²⁷ because the introduced

surface hydroxyl groups on TiO₂ remarkably enhanced HCHO adsorption *via* strong hydrogen-bond interactions.

Since the first discovery of its unexpected photocatalytic activity in 2011,²⁸ hydrogenated TiO₂ (H-TiO₂) has attracted great attention in catalysis, as either an active component or a support.^{29,30} Effective hydrogen doping into pristine TiO₂ can result in surprising structural and chemical alterations, such as abundant hydroxyls and oxygen vacancies on surface, and tunable band states with metallic features.^{31–34} Due to the fact that surface hydroxyls can strengthen HCHO chemisorption,^{27,34} such surface variations on H-TiO₂ are highly anticipated to promote the catalytic oxidation of HCHO. Zeng *et al.* identified promoted HCHO oxidation on H-TiO₂,³⁵ which however was used as the active species and thereby delivered a relatively lower activity in comparison with supported noble-metals. Moreover, H-TiO₂ with enriched d band states around the Fermi level (E_F)²⁸ would even modify the reactivity of loaded metals through electronic perturbations,³⁶ leading to a more efficient catalytic turnover.

Herein, we developed nanosized H-TiO₂ as reactive supports to enhance the catalytic oxidation of HCHO on Ir nanocatalysts. Upon a solid-state reduction by NaBH₄,³⁷ the as-obtained H-TiO₂ nanoparticles feature enriched surface hydroxyls and enhanced electronic interactions upon loading Ir. As expected, the Ir/H-TiO₂ is more active than the Ir/TiO₂ counterpart in HCHO oxidation to CO₂ and H₂O. It also affords a satisfactory stability in a long-term continuous test. An *in situ* diffuse reflectance infrared Fourier transform spectroscopy (DRIFTS) study further reveals the generation of HCOO⁻ on Ir/H-TiO₂, which is believed to be the rate-determining step in HCHO oxidation. The abundant hydroxyls on H-TiO₂ can help enhance HCHO chemisorption and thus promote formate generation.

Department of Chemistry, College of Chemistry and Materials Science, Jinan University, Guangzhou 510632, China. E-mail: tqsgao@jnu.edu.cn

† Electronic supplementary information (ESI) available: UV-vis DRS, FT-IR and N₂ sorption isotherms of H-TiO₂ and TiO₂, CO-DRIFTS and CO-TPD of Ir/H-TiO₂ and Ir/TiO₂, and catalytic performance of the counterparts of Ir and Pt catalysts. See DOI: 10.1039/c8nj04472d

At the same time, the electronic metal–support interactions arising from H-TiO₂ facilitate intermediate conversion. Thereby, Ir/H-TiO₂ affords favored kinetics and improved catalytic activity. Elucidating the clear promotion by hydrogenated metal oxide supports, this work will open up new opportunities to design high-performance heterogeneous catalysts *via* support engineering.

Results and discussion

In comparison with the reduction by high-pressure H₂ or high-temperature Al vapor,^{28,38} a recently developed route using NaBH₄ is obviously facile and easy in operation.³⁷ It is thus adopted in this work to reduce white TiO₂ to black H-TiO₂, and the residual NaBH₄ and derivatives are removed after soaking in deionized water. The UV-vis diffuse reflection spectra (UV-vis DRS) accordingly show a broad absorption for the as-obtained samples, starting at ~400 nm and extending to the near infrared region (Fig. S1, ESI†). This is consistent with the color change of the samples (insets of Fig. 1a and b), and suggests the successful fabrication of H-TiO₂. Fig. 1a and b display the scanning electron microscopy (SEM) images of the parent TiO₂ and the as-obtained H-TiO₂, respectively, in which similar nanoparticles with a size of tens of nanometers are observed. It is implied that the reduction by NaBH₄ causes a negligible alteration on the nanostructures. Meanwhile, the X-ray diffraction (XRD) pattern of the H-TiO₂ shows a rutile phase (JCPDS No. 12-1276), which is consistent with that of the TiO₂ (Fig. 1c). However, the relatively weaker diffraction peaks for the H-TiO₂ still indicate the degradation of the crystalline structures. The resulting structural defects will be responsible for the slightly

higher BET surface area of H-TiO₂ (42.4 m² g⁻¹) than that of TiO₂ (28.8 m² g⁻¹, Fig. S2, ESI†).

X-ray photoelectron spectroscopy (XPS) was further conducted to understand the surface variation of TiO₂ after NaBH₄ reduction. The H-TiO₂ (Fig. 1d) presents two peaks associated with Ti 2p_{3/2} (458.3 eV) and Ti 2p_{1/2} (464.0 eV),^{39,40} which are slightly red-shifted in comparison with those for TiO₂ (458.6 and 464.3 eV). This indicated that the surface Ti⁴⁺ species is partially reduced, in good accordance with the previous reports.³⁷ Meanwhile, the O 1s profiles can be deconvoluted into three peaks (Fig. 1e). The peaks at 530.0 and 531.0 eV are ascribed to the oxygen in the TiO₂ lattice (Ti–O–Ti) and the surface hydroxyls (Ti–OH),^{23,34,41} respectively, and the one at 532.8 eV is associated with the O 1s from the SiO₂ impurity existing in the TiO₂ precursor.⁴² SiO₂ purity is inert in catalysis, and can be drastically removed in NaBH₄ aqueous solutions.⁴³ Both of XPS (Fig. 1e) and X-ray fluorescence (Table S1, ESI†) measurements show the obvious decrease of the SiO₂ content in H-TiO₂. Thus, SiO₂ impurity is ignored in the following discussion. Remarkably, the H-TiO₂ presents the more obvious signal for the O 1s of Ti–OH, indicating the enriched hydroxyls on the H-TiO₂ surface. As determined by quantitative XPS analysis, the value of O_{Ti–OH}/O_{lattice} increases from 0.21 on TiO₂ to 0.38 on H-TiO₂, agreeing with the observation in ref. 28.

The above variation can be further confirmed by Fourier transform infrared (FT-IR) spectroscopy (Fig. S3, ESI†). The visible band at 3700 cm⁻¹, associated with the O–H stretching vibration, is observable for H-TiO₂, but negligible for TiO₂. Meanwhile, we performed TPO analysis on both TiO₂ and H-TiO₂ (Fig. 1f), which confirms the above-mentioned variations on the surface. The TiO₂ presents a negligible signal in the range of 30–700 °C. By contrast, the H-TiO₂ shows an obvious oxidation peak

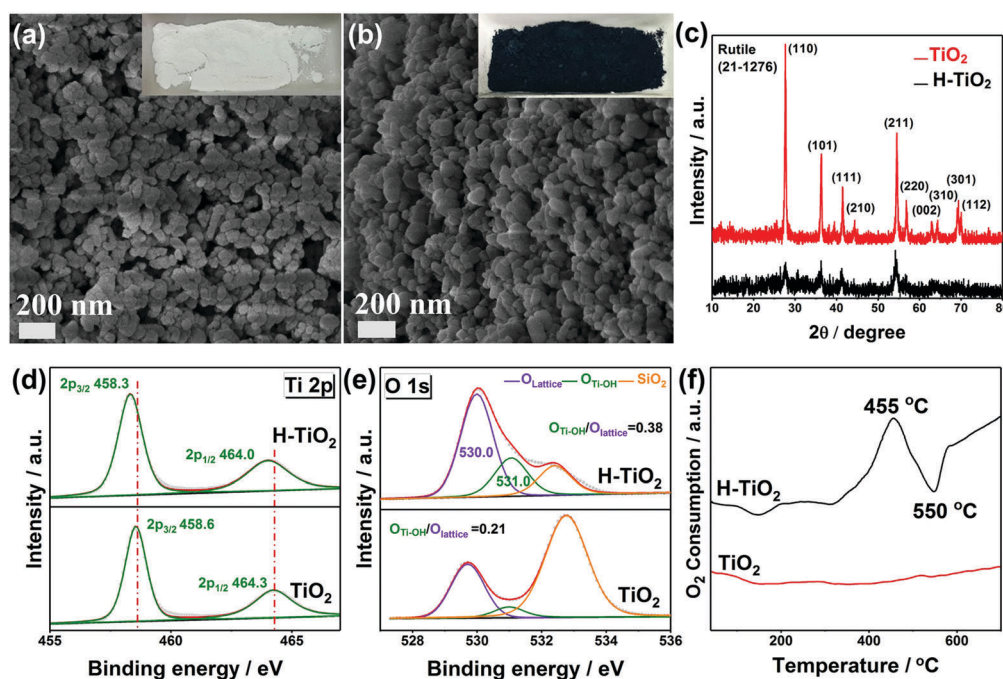


Fig. 1 SEM images of (a) TiO₂ and (b) H-TiO₂ and (insets of a and b) the corresponding digital photos. (c) XRD patterns. (d) Ti 2p and (e) O 1s XPS profiles of H-TiO₂ and TiO₂. (f) TPO profiles of H-TiO₂ and TiO₂.

at 455 °C. And a negative peak at around 550 °C observed for H-TiO₂ is possibly due to the dehydration from the surface hydroxyls.

Using a typical impregnation procedure, Ir nanoparticles were successfully loaded onto TiO₂ and H-TiO₂. The transmission electron microscopy (TEM) images of the Ir/TiO₂ and Ir/H-TiO₂ with a similar Ir loading (0.8 ± 0.1 wt%) are displayed in Fig. 2a and b, respectively. The Ir nanoparticles (as marked in the TEM images) present a consistent distribution, with an average size of 2.0 ± 0.1 nm. Such highly dispersed metallic Ir is beneficial for the catalytic performance. Meanwhile, the lattice fringes of 0.32 and 0.22 nm observed in their high-resolution TEM images (HR-TEM, Fig. 2c and d) can be ascribed to rutile TiO₂(110) and Ir(111), respectively. Moreover, the above samples were analyzed by means of energy dispersive spectroscopy (EDS) and elemental mapping in conjunction with TEM. The EDS profiles clearly reveal the presence of Ti, O, and Ir, and the signal for Cu should be ascribed to the supporting grid used in TEM (Fig. S4, ESI[†]). The elemental mapping images show the uniform distribution of Ti, O, and Ir (Fig. 2e and f), confirming the good dispersion of Ir on both TiO₂ and H-TiO₂ supports.

H₂ temperature-programmed reduction (H₂-TPR) was conducted to investigate the metal-support interactions in Ir/TiO₂ and Ir/H-TiO₂. As shown in Fig. 3a, the H₂IrCl₆/TiO₂ presents a series of peaks at 162 °C, 197 °C, 246 °C and 418 °C. According to the previous reports, the reduction of Ir⁴⁺ species usually occurs below 300 °C.^{44,45} Thus, the H₂ consumption at 418 °C is possibly associated with the species stabilized by the TiO₂ supports. In comparison, the H₂IrCl₆/H-TiO₂ clearly presents H₂

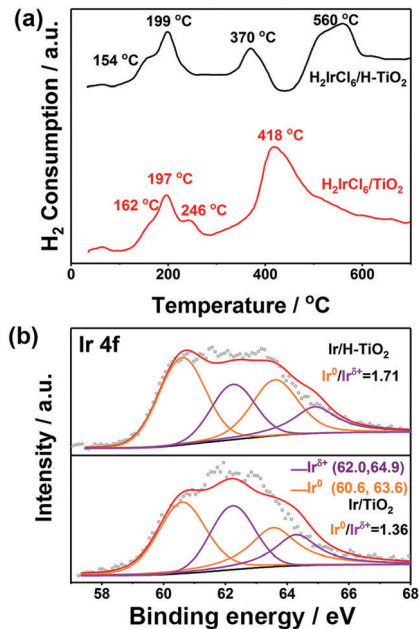


Fig. 3 (a) H₂-TPR profiles of H₂IrCl₆/H-TiO₂ and H₂IrCl₆/TiO₂. (b) Ir 4f XPS profiles for 0.9% Ir/TiO₂ and 0.7% Ir/H-TiO₂.

consumption for Ir⁴⁺ reduction at 154 °C, 199 °C, and 370 °C, lower than those on TiO₂. Such a relatively easier reduction at a lower temperature indicates the enhanced metal-support interactions arising from H-TiO₂. In addition, a new peak is observed at 560 °C, which is possibly ascribed to the H₂ spillover from the *in situ* generated Ir to the defect-rich H-TiO₂ surface.⁴⁶

Metal-support interactions were further interpreted by XPS and CO-DRIFTS. The XPS analysis shows the chemical state of Ir affected by the H-TiO₂ and TiO₂ supports. As shown in Fig. 3b, the Ir 4f profiles are deconvoluted into four peaks, indicating the presence of two states of Ir on the surface. The peaks located at 60.6 and 63.6 eV are ascribed to 4f_{7/2} and 4f_{5/2} of metallic Ir⁰, respectively, and those at 62.0 and 64.9 eV are associated with the positively charged Ir (Ir^{δ+}).⁴⁷ According to the XPS quantitative analysis, the Ir/H-TiO₂ presents a slightly higher Ir⁰/Ir^{δ+} ratio (1.71) than that of Ir/TiO₂ (1.36). Previous theoretical calculations have attested that the enriched band states around the E_F after introducing H into TiO₂,²⁸ and the consequently down-shifted d-band center will be beneficial for electron penetration into Ir.⁴⁸ Wang and co-workers have discovered strong interactions between single-atomic Au and defective TiO₂ nanosheets, which however promoted the formation of Au^{δ+} species.⁴⁹ This different observation was possibly associated with the single-atom nature. And in this work, the Ir nanoparticles with a size of ~2.0 nm suffer from charge redistribution on the interfaces with H-TiO₂, resulting in a slightly increasing metallic Ir⁰ content. Moreover, the CO-DRIFTS spectra present the consistent interactions on H-TiO₂ (Fig. S5, ESI[†]). The Ir/H-TiO₂ presents two absorption bands at 1660 and 2000 cm⁻¹, associated with the C=O stretching in the linear- and bridge-type CO on the Ir sites,⁵⁰ respectively. These bands visibly red-shift in comparison with those for Ir/TiO₂ (1730 and 2040 cm⁻¹). The higher Ir⁰/Ir^{δ+} on Ir/H-TiO₂ determined

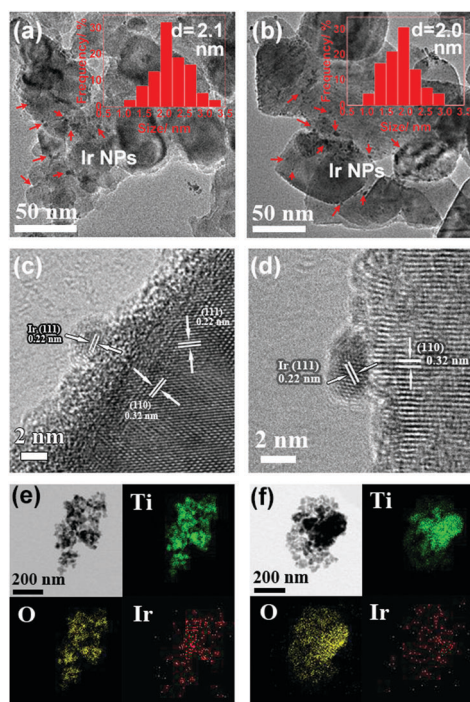


Fig. 2 (a and b) TEM and (c and d) HR-TEM images of (a and c) 0.9% Ir/TiO₂ and (b and d) 0.7% Ir/H-TiO₂, and (e and f) the corresponding elemental mapping (e: 0.9% Ir/TiO₂; f: 0.7% Ir/H-TiO₂). The Ir nanoparticles are marked in the TEM images.

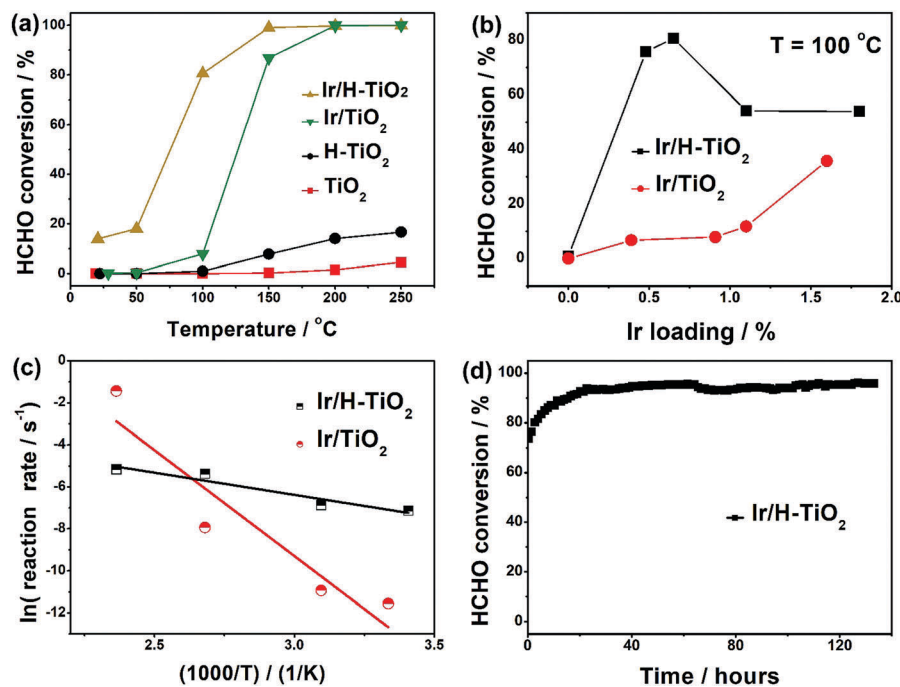


Fig. 4 (a) Catalytic HCHO oxidation on Ir/TiO₂, Ir/H-TiO₂, TiO₂ and H-TiO₂ at different temperatures, and (b) the performance relying on the Ir loading at 100 °C. (c) Arrhenius plots of 0.7% Ir/H-TiO₂ and 0.9% Ir/TiO₂. (d) HCHO oxidation on 0.7% Ir/H-TiO₂ at 120 °C with time of stream.

by XPS indicates more electrons in the Ir sites, as compared with Ir/TiO₂. Thereby, the improved electronic density on the Ir sites will promote electron feedback from d_{Ir} to 2π*_{C=O}, which weakens the C=O bond and contributes to its red-shift in the DRIFTS spectra.⁵¹

The catalytic HCHO oxidation was examined on TiO₂, H-TiO₂, Ir/TiO₂ and Ir/H-TiO₂. Fig. 4a displays the HCHO conversion as a function of reaction temperature. Both of TiO₂ and H-TiO₂ present a negligible activity in the temperature range of 50–250 °C. After loading Ir, the catalysts show an obvious improvement in the HCHO conversion, confirming Ir to be the main active species. Only the oxidation products CO₂ and H₂O are detected in this reaction. Remarkably, the Ir/H-TiO₂ enables much higher HCHO conversion than Ir/TiO₂, which suggests the promotion due to H-TiO₂ that features abundant surface hydroxyls and enhanced metal–support interactions.

The Ir loading on TiO₂ and H-TiO₂ was further monitored to optimize their catalytic performance, in which their activity at 100 °C was taken for comparison. Visibly, there is a maximum HCHO conversion on the Ir/H-TiO₂ with an optimal Ir loading of 0.7%, reaching almost complete conversion at a space velocity of 20 000 h⁻¹. The above volcano plot is consistent with the quantitative CO desorption from Ir/H-TiO₂ (Fig. S6a and b, ESI[†]), indicating that the high Ir dispersity resulting from the optimized metal–support interactions accounts for the efficient catalytic turnover. By contrast, the Ir/TiO₂ delivers the improved activity with increasing Ir loading, which is always inferior to that of Ir/H-TiO₂. This trend is consistent with the increasing CO desorption in the CO-TPD analysis (Fig. S6c and d, ESI[†]).

Furthermore, the kinetics on Ir/TiO₂ and Ir/H-TiO₂ was studied with an assumption of pseudo-first order reaction in HCHO oxidation.⁵² Fig. 4c shows the plots of the logarithm of

reaction rates against the reciprocal temperature (300–473 K), in which all the loaded Ir is assumed to contribute to the catalytic oxidation. As determined, the Ir/H-TiO₂ shows a lower *E*_a of 2.5 kJ mol⁻¹, in comparison with that of Ir/TiO₂ (12.1 kJ mol⁻¹). This is in agreement with the high activity for HCHO oxidation on the Ir/H-TiO₂, and also illustrates the improved intrinsic activity of Ir on the H-TiO₂ supports.

Moreover, the Ir/H-TiO₂ also affords a satisfactory stability in HCHO oxidation (Fig. 4d). It shows negligible deactivation in a continuous test for more than 140 hours. The HCHO conversion is maintained above 95%. The Ir/H-TiO₂ after reaction is further characterized (Fig. S7, ESI[†]). The negligible variation in the crystalline structure of H-TiO₂ is confirmed by XRD analysis. And XPS analysis reveals the well-retained chemical states of the elements (Ti, O and Ir) after reactions, which contribute to the high activity in the long-term test.

To understand the promotion by the H-TiO₂ support, an *in situ* DRIFTS test was performed over Ir/TiO₂ and Ir/H-TiO₂ (Fig. 5a and b). The catalysts are exposed to gaseous O₂/N₂ containing 48 ppm HCHO at 30 °C, and then DRIFTS spectra were recorded after different times. On the Ir/H-TiO₂, the observable band at 1530 cm⁻¹ can be ascribed to the vibration of COO⁻ in formate, indicating the HCHO oxidation *via* the formate intermediate.^{12,53} And the bands corresponding to the linear and bridged modes of CO chemisorption on Ir emerge with reaction time, which indicates the further reaction of formate into CO *via* dehydration.⁵⁴ By contrast, the band for COO⁻ is negligible on the Ir/TiO₂ (Fig. 5b), implying a different reaction pathway on Ir/H-TiO₂. Along the reaction time, the bands for C=O adsorbed on the Ir surface are observed,⁵⁵ which should be generated from the direct dehydrogenation of HCHO on Ir.

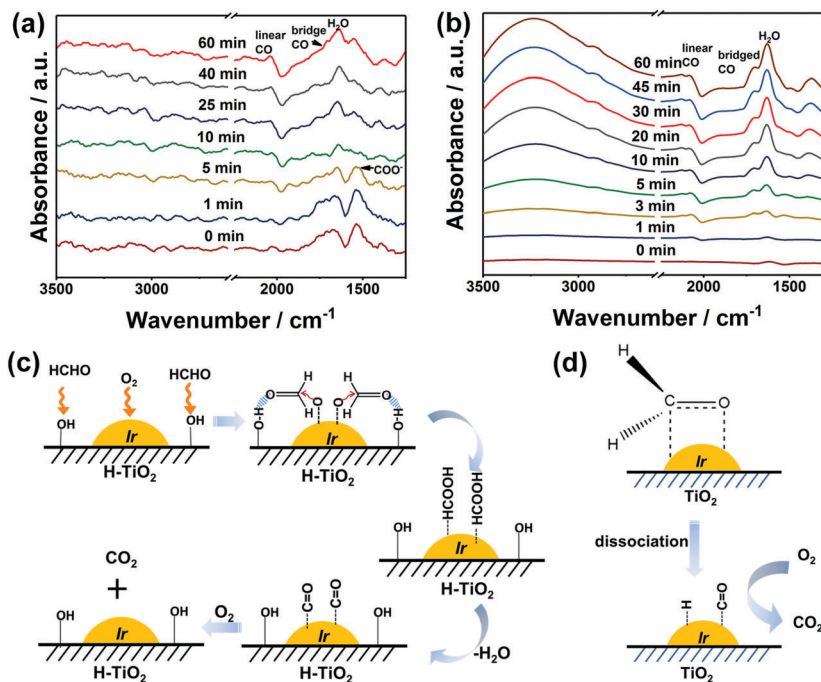


Fig. 5 *In situ* HCHO-DRIFTS of (a) 0.9% Ir/TiO₂ and (b) 0.7% Ir/H-TiO₂ after being exposed to a gas mixture of 48 ppm HCHO + N₂ + O₂. Schematic illustrations of the reaction pathway for HCHO oxidation on (c) Ir/H-TiO₂ and (d) Ir/TiO₂.

For HCHO oxidation, the hydroxyl groups on the catalyst surface play a key role in the generation of the formate intermediate that has been identified on Ir/H-TiO₂ by DRIFTS. We, therefore, propose a reaction mechanism as depicted in Fig. 5c. The hydroxyls on H-TiO₂ will promote the chemisorption of HCHO *via* strong hydrogen-bonding interactions, and the atomic O* on the Ir surface from O₂ dissociation will attack the chemisorbed HCHO, subsequently producing the formate intermediate. After formate dehydration, CO* is formed on the Ir surface, and is further oxidized by the O* *via* the Mars-van Krevelen (MvK) mechanism.^{12,56} Because of the formate intermediate, the HCHO oxidation kinetics is well promoted, as indicated by the relatively low *E_a*. In comparison, Ir/TiO₂ suffers from a disfavored kinetics due to the absence of rich surface hydroxyls (Fig. 5d). In addition, the metal-support interactions enhanced by H-TiO₂ have enriched main metallic species on Ir nanoparticles, which not only promote the formation and dehydration of the formate intermediate, but also activate O₂ to form highly active O*. This feature is beneficial for the oxidation of HCHO.

The promotion by surface hydroxyls in HCHO oxidation can be further confirmed by control experiments where NaOH is used to modify TiO₂ supports. As indicated by XPS analysis (Fig. S8, ESI[†]), such a modification results in enriched -OH on the TiO₂ surface. Accordingly, the Ir supported by NaOH-treated TiO₂ enables an obviously improved HCHO conversion in comparison with Ir/TiO₂. This is in accordance with the previously reported Pt/TiO₂ catalysts.²⁷

As reactive supports, the H-TiO₂ can also enhance HCHO oxidation on other metals, *e.g.*, Pt, which highlights its surface/interfacial functionalities. The Pt/H-TiO₂ delivers superior activity for HCHO oxidation to Pt/TiO₂ (Fig. S9, ESI[†]). This is

owing to the enhanced chemisorption of HCHO by the rich surface hydroxyls on H-TiO₂. Meanwhile, the Pt/H-TiO₂ retains a higher Pt⁰/Pt^{δ+} surface ratio (2.90) than Pt/TiO₂ (2.65) due to the enhanced metal-support interactions by H-TiO₂. This also benefits the activation of O₂.

Conclusions

In summary, black H-TiO₂ nanoparticles with rich surface hydroxyls were fabricated and utilized as robust supports for Ir, accomplishing the obviously improved activity for HCHO oxidation. In comparison with the parent TiO₂, the H-TiO₂ features enriched surface hydroxyls and enhanced metal-support interactions upon loading Ir, which are responsible for the remarkable improvement in the catalytic performance. The abundant hydroxyls on H-TiO₂ can enhance HCHO chemisorption and formate formation, and the enhanced metal-support interactions associated with H-TiO₂ facilitate the further conversion of the intermediates. Thereby, the Ir/H-TiO₂ affords favored kinetics and improved catalytic activity. In future work, such innovation can be extended to mesoporous H-TiO₂ with large surface areas and rich mesoporosity, accomplishing further improvement in catalysis. This work is anticipated to open up new opportunities for the exploration of high-performance materials in catalysis and environmental science.

Experimental

Materials

All reagents were purchased from commercial sources and in analytical or reagent grade when possible. TiO₂ and H₂IrCl₆

were purchased from Aladdin Industrial Corporation (Shanghai, China). NaBH₄, ethanol and formaldehyde solution were purchased from Sinopharm Chemical Reagent Co. Ltd (Shanghai, China). All aqueous solutions were prepared using ultrapure water (>18.2 MΩ).

Synthesis of the catalyst

The H-TiO₂ nanoparticles were fabricated according to the previous report.³⁷ Typically, 1.0 g of TiO₂ was mixed with 1.2 g of NaBH₄, and then heated at 350 °C for 1 hour under an Ar flow. NaBH₄ is in excess to ensure the effective hydrogenation of TiO₂. The as-obtained black solid was soaked in deionized water for 3 days. And then, H-TiO₂ was obtained after centrifugation. To fabricate Ir/H-TiO₂, Ir/TiO₂, Pt/H-TiO₂ and Pt/TiO₂, the corresponding supports were impregnated with an H₂IrCl₆ or H₂PtCl₆ aqueous solution and then stirred at 80 °C for 4 hours. The samples were dried at 50 °C under vacuum overnight, followed by reduction with a stream of H₂/Ar (5 vol%) at 300 °C for 2 hours.

In a control experiment using NaOH to modify TiO₂, 1.0 g of TiO₂ was added into 100 mL of a NaOH solution (0.5 M) under stirring for 30 min. And then, the solid was filtered and dried at 80 °C for 6 hours. To load Ir nanoparticles, the same procedure as that used for Ir/H-TiO₂ was adopted.

Physical measurements

X-ray diffraction (XRD) measurements were performed on a Bruker D8 powder X-ray diffractometer with Cu Kα radiation (λ = 0.15419 nm). Scanning electron microscopy (SEM) and transmission electron microscopy (TEM) investigations were carried out using ZEISS ULTRA55 and JEOL JEM-2100F, respectively. Energy dispersive spectroscopy (EDS) coupled with TEM was carried out on a JEOL JEM-2100F. X-ray photoelectron spectroscopy (XPS) analysis was performed on a Thermo scientific Escalab 250Xi, with C 1s (284.6 eV) as a reference. The UV-vis diffuse reflection spectra (UV-vis DRS) were recorded on a Varian Cary 5000 at room temperature. The Brunauer-Emmett-Teller (BET) specific surface areas were determined by N₂ adsorption-desorption measurements at liquid nitrogen temperature, using a Quantachrome autosorb iQ2 automatic gas adsorption analyzer. H₂ temperature-programmed reduction (H₂-TPR), CO temperature-programmed desorption (CO-TPD), and temperature-programmed oxidation (TPO) were conducted by using a Quantachrome ChemBET Pulsar. DRIFTS was performed on a Nicolet 6700 device with an MCT-A detector, and scanned from 4000 to 650 cm⁻¹ with 32 scans at a resolution of 4 cm⁻¹. In CO-DRIFTS study, the sample was pre-treated at 200 °C using He for 1 hour, and then a gas mixture of 5 vol% CO/He was introduced at a rate of 40 mL min⁻¹ at 30 °C for 1 hour. The He flow was then switched into the system before date recording. In *in situ* HCHO-DRIFTS study, the sample was pre-treated at 300 °C using He for 1 hour. After the introduction of a 20 vol% O₂/N₂ mixture containing 48 ppm HCHO at a flow rate of 30 mL min⁻¹ at 30 °C for 1 hour, the spectra were recorded at different times.

Catalytic tests

The formaldehyde oxidation reaction was carried out in a fixed bed quartz tube reactor (id = 5 mm) with 0.2 g of catalysts (40–60 mesh). HCHO was produced by passing a stream of 99.999% N₂ through a bubbler containing a 40 wt% HCHO aqueous solution in a 25 °C water bath. The total flow of gas was 100 mL min⁻¹, containing around 580 ppm of formaldehyde balanced by 21% O₂/N₂. The space velocity was accordingly 20 000 h⁻¹. The conversion of HCHO was analysed using a gas chromatograph (FL9790 II). For kinetics analysis, the apparent activation energies (*E_a*) for oxidation over Ir/H-TiO₂ and Ir/TiO₂ were calculated by the Arrhenius equation, with an assumption that all of the Ir contributes to the catalytic oxidation.

Conflicts of interest

There are no conflicts to declare.

Acknowledgements

This work is financially supported by the National Natural Science Foundation of China (Grant No. 21773093 and 21433002), the Guangdong Natural Science Funds for Distinguished Young Scholar (Grant No. 2015A030306014), the Guangdong Program for Support of Top-notch Young Professionals (Grant No. 2014TQ01N036), and the Science and Technology Program of Guangzhou (Grant No. 201707010268).

Notes and references

- 1 T. Salthammer, S. Mentese and R. Marutzky, *Chem. Rev.*, 2010, **110**, 2536–2572.
- 2 S. Suresh and T. J. Bandosz, *Carbon*, 2018, **137**, 207–221.
- 3 A. Yusuf, C. Snape, J. He, H. Xu, C. Liu, M. Zhao, G. Z. Chen, B. Tang, C. Wang, J. Wang and S. N. Behera, *Catal. Rev.*, 2017, **59**, 189–233.
- 4 L. Wu, Z. Qin, L. Zhang, T. Meng, F. Yu and J. Ma, *New J. Chem.*, 2017, **41**, 2527–2533.
- 5 J. Yang, Q. Shi, R. Zhang, M. Xie, X. Jiang, F. Wang, X. Cheng and W. Han, *Carbon*, 2018, **138**, 118–124.
- 6 B. Bai, Q. Qiao, J. Li and J. Hao, *Chin. J. Catal.*, 2016, **37**, 102–122.
- 7 J. Q. Torres, S. Royer, J. P. Bellat, J. M. Giraudon and J. F. Lamonier, *ChemSusChem*, 2013, **6**, 578–592.
- 8 G. J. Kim, S. M. Lee, S. C. Hong and S. S. Kim, *RSC Adv.*, 2018, **8**, 3626–3636.
- 9 S. Song, X. Wu, C. Lu, M. Wen, Z. Le and S. Jiang, *Appl. Surf. Sci.*, 2018, **442**, 195–203.
- 10 F. Xu, Y. Le, B. Cheng and C. Jiang, *Appl. Surf. Sci.*, 2017, **426**, 333–341.
- 11 J. Ding, Z. Rui, L. Pintian, Y. Liu, X. Liu and H. Ji, *Appl. Surf. Sci.*, 2018, **457**, 670–675.
- 12 D. Sun, Y. Le, C. Jiang and B. Cheng, *Appl. Surf. Sci.*, 2018, **441**, 429–437.
- 13 L. Nie, J. Yu and J. Fu, *ChemCatChem*, 2014, **6**, 1983–1989.

- 14 V. Cherepakhin and T. J. Williams, *ACS Catal.*, 2018, **8**, 3754–3763.
- 15 Y. Zhang, C. Wu, H. Jiang, Y. Lin, H. Liu, Q. He, S. Chen, T. Duan and L. Song, *Adv. Mater.*, 2018, **30**, 1707522.
- 16 Z. Liu, X. Tan and C. Lv, *Appl. Surf. Sci.*, 2013, **283**, 290–296.
- 17 S. Imamura, Y. Uematsu, K. Utani and T. Ito, *Ind. Eng. Chem. Res.*, 1991, **30**, 18–21.
- 18 T. Yang, Y. Huo, Y. Liu, Z. Rui and H. Ji, *Appl. Catal., B*, 2017, **200**, 543–551.
- 19 X. Yu, J. He, D. Wang, Y. Hu, H. Tian and Z. He, *J. Phys. Chem. C*, 2011, **116**, 851–860.
- 20 F. Chen, F. Wang, Q. Li, C. Cao, X. Zhang, H. Ma and Y. Guo, *Catal. Commun.*, 2017, **99**, 39–42.
- 21 S. Colussi, M. Boaro, L. de Rogatis, A. Pappacena, C. de Leitenburg, J. Llorca and A. Trovarelli, *Catal. Today*, 2015, **253**, 163–171.
- 22 X. Tang, J. Chen, X. Huang, Y. Xu and W. Shen, *Appl. Catal., B*, 2008, **81**, 115–121.
- 23 T. Lv, C. Peng, H. Zhu and W. Xiao, *Appl. Surf. Sci.*, 2018, **457**, 83–92.
- 24 Y. Duan, S. Song, B. Cheng, J. Yu and C. Jiang, *Chin. J. Catal.*, 2017, **38**, 199–206.
- 25 Z. Xu, J. Yu and M. Jaroniec, *Appl. Catal., B*, 2015, **163**, 306–312.
- 26 H. Huang, P. Hu, H. Huang, J. Chen, X. Ye and D. Y. C. Leung, *Chem. Eng. J.*, 2014, **252**, 320–326.
- 27 L. Nie, J. Yu, X. Li, B. Cheng, G. Liu and M. Jaroniec, *Environ. Sci. Technol.*, 2013, **47**, 2777–2783.
- 28 X. Chen, L. Liu, P. Y. Yu and S. S. Mao, *Science*, 2011, **331**, 746–750.
- 29 W. Zhou, W. Li, J. Q. Wang, Y. Qu, Y. Yang, Y. Xie, K. Zhang, L. Wang, H. Fu and D. Zhao, *J. Am. Chem. Soc.*, 2014, **136**, 9280–9283.
- 30 L. Li, L. Song, L. F. Zhu, Z. Yan and X. B. Cao, *Catal. Sci. Technol.*, 2018, **8**, 1277–1287.
- 31 M. Tian, M. Mahjouri-Samani, G. Eres, R. Sachan, M. Yoon, M. F. Chisholm, K. Wang, A. A. Puretzky, C. M. Rouleau, D. B. Geohegan and G. Duscher, *ACS Nano*, 2015, **9**, 10482–10488.
- 32 T. Xia and X. Chen, *J. Mater. Chem. A*, 2013, **1**, 2983–2989.
- 33 M. I. Nandasiri, V. Shutthanandan, S. Manandhar, A. M. Schwarz, L. Oxenford, J. V. Kennedy, S. Thevuthasan and M. A. Henderson, *J. Phys. Chem. Lett.*, 2015, **6**, 4627–4632.
- 34 D. Liu, M. Zhang, W. Xie, L. Sun, Y. Chen and W. Lei, *Appl. Catal., B*, 2017, **207**, 72–78.
- 35 L. Zeng, W. Song, M. Li, D. Zeng and C. Xie, *Appl. Catal., B*, 2014, **147**, 490–498.
- 36 K. Fujiwara, K. Okuyama and S. E. Pratsinis, *Environ. Sci.: Nano*, 2017, **4**, 2076–2092.
- 37 H. Tan, Z. Zhao, M. Niu, C. Mao, D. Cao, D. Cheng, P. Feng and Z. Sun, *Nanoscale*, 2014, **6**, 10216–10223.
- 38 Z. Wang, C. Yang, T. Lin, H. Yin, P. Chen, D. Wan, F. Xu, F. Huang, J. Lin, X. Xie and M. Jiang, *Adv. Funct. Mater.*, 2013, **23**, 5444–5450.
- 39 F. Liu, P. Xiao, W. Q. Tian, M. Zhou, Y. Li, X. Cui, Y. Zhang and X. Zhou, *Phys. Chem. Chem. Phys.*, 2015, **17**, 28626–28634.
- 40 H. Zhang, F. Liu, H. Wu, X. Cao, J. Sun and W. Lei, *RSC Adv.*, 2017, **7**, 40327–40333.
- 41 T. Leshuk, R. Parviz, P. Everett, H. Krishnakumar, R. A. Varin and F. Gu, *ACS Appl. Mater. Interfaces*, 2013, **5**, 1892–1895.
- 42 T. Gross, M. Ramm, H. Sonntag and W. Unger, *Surf. Interface Anal.*, 1992, **18**, 59–64.
- 43 T. Zhang, J. Ge, Y. Hu, Q. Zhang, S. Aloni and Y. Yin, *Angew. Chem., Int. Ed.*, 2008, **47**, 5806–5811.
- 44 S. He, L. F. Xie, M. W. Che, H. C. Chan, L. C. Yang, Z. P. Shi, Y. Tang and Q. S. Gao, *J. Mol. Catal. A: Chem.*, 2016, **425**, 248–254.
- 45 S. He, Z. J. Shao, Y. J. Shu, Z. P. Shi, X. M. Cao, Q. S. Gao, P. J. Hu and Y. Tang, *Chem. – Eur. J.*, 2016, **22**, 5698–5704.
- 46 E. W. Zhao, H. Zheng, K. Ludden, Y. Xin, H. E. Hagelin-Weaver and C. R. Bowers, *ACS Catal.*, 2016, **6**, 974–978.
- 47 W. Feng, G. Wu, L. Li and N. Guan, *Green Chem.*, 2011, **13**, 3265–3272.
- 48 L. Xie, T. Chen, H. C. Chan, Y. Shu and Q. Gao, *Chem. – Asian J.*, 2018, **13**, 641–647.
- 49 J. Wan, W. Chen, C. Jia, L. Zheng, J. Dong, X. Zheng, Y. Wang, W. Yan, C. Chen, Q. Peng, D. Wang and Y. Li, *Adv. Mater.*, 2018, **30**, 1705369.
- 50 J. C. Matsubu, S. Zhang, L. DeRita, N. S. Marinkovic, J. G. Chen, G. W. Graham, X. Pan and P. Christopher, *Nat. Chem.*, 2016, **9**, 120–127.
- 51 G. Liang, L. He, M. Arai and F. Zhao, *ChemSusChem*, 2014, **7**, 1415–1421.
- 52 R. Dewil, K. Everaert and J. Baeyens, *Catal. Commun.*, 2005, **6**, 793–795.
- 53 Y. Huang, W. Fan, B. Long, H. Li, W. Qiu, F. Zhao, Y. Tong and H. Ji, *J. Mater. Chem. A*, 2016, **4**, 3648–3654.
- 54 S. Huang, X. Zhu, B. Cheng, J. Yu and C. Jiang, *Environ. Sci.: Nano*, 2017, **4**, 2215–2224.
- 55 H.-C. Wu, T.-C. Chen, Y.-C. Chen, J.-F. Lee and C.-S. Chen, *J. Catal.*, 2017, **355**, 87–100.
- 56 L. Nie, J. Yu, M. Jaroniec and F. F. Tao, *Catal. Sci. Technol.*, 2016, **6**, 3649–3669.